Chinese Chemical Letters 34 (2023) 108410

Contents lists available at ScienceDirect

Chinese Chemical Letters

journal homepage: www.elsevier.com/locate/cclet

Effective and selective electrocatalytic nitrate reduction to ammonia on urchin-like and defect-enriched titanium oxide microparticles

Mue Tang[a,1], Qiuwen Tong[b,1], Yiming Li[b], Ruchun Jiang[a], Li Shi[b], Fei Shen[b], Yali Wei[c], Zixun Liu[b], Shuyue Liu[a], Jun Zhang[a,*], Guangming Jiang[b,*]

[a] College of Metallurgy and Materials Engineering, Chongqing Key Laboratory of Nano/Micro Composites and Devices, Chongqing University of Science and Technology, Chongqing 401331, China
[b] Engineering Research Center for Waste Oil Recovery Technology and Equipment, Ministry of Education, Chongqing Technology and Business University, Chongqing 400067, China
[c] Sichuan Academy of Environmental Sciences, Chengdu 610041, China

ARTICLE INFO

Article history:
Received 1 December 2022
Revised 3 March 2023
Accepted 29 March 2023
Available online 31 March 2023

Keywords:
Nitrate pollution
TiO_2
Electrocatalytic nitrate reduction
Oxygen vacancy
Ammonia selectivity

ABSTRACT

This work reported a facile approach to surface oxygen vacancy (O_V)-enriched urchin-like TiO_2 microparticles (U-TiO_2), which were highly effective and durable in catalyzing selective nitrate reduction to ammonia (NO_3RR). Specifically, the U-TiO_2 delivered a mass activity of 1.15 min^{-1} $mg^{-1}_{catalyst}$, a low yield of toxic NO_2^--N intermediate (≤0.4 mg/L) and an exceptional high NH_3-N selectivity of 98.1% in treating 22.5 mg/L of NO_3^--N under a potential of -0.60 V *vs.* RHE, outperforming most of the reported oxide-based catalysts. When comparing the performance of U-TiO_2 with that of the solid amorphous TiO_2 counterpart (A-TiO_2) that had close particle size but more O_V on surfaces, we identified that the O_V was the reactive sites, but rather than its content, the NO_3RR kinetics were primarily limited by the electron and mass transfer at U-TiO_2/water interfaces. Accordingly, the superior performance of U-TiO_2 to A-TiO_2 could be ascribed to the hierarchical urchin-like structure in U-TiO_2. The *in-situ* DEMS test revealed that the NO_3RR on U-TiO_2 followed a pathway of $^*NO_3^- \rightarrow {}^*NO_2^- \rightarrow {}^*NO \rightarrow {}^*N \rightarrow {}^*NH \rightarrow {}^*NH_2 \rightarrow {}^*NH_3$. We also demonstrated that the U-TiO_2 could keep its robust performance under a wide NO_3^--N concentration range and in the presence of some co-existing ions (such as Ca^{2+}, Cl^-, Mg^{2+}). However, the presence of humic acid and CO_3^{2-} in water slowed down the NO_3RR on U-TiO_2. This work provides a more fundamental insight into the O_V-driven NO_3RR process on TiO_2, which should benefit for the development of efficient TiO_2-based catalysts.

Nitrate pollution in surface water and underground aquifer has been increasingly serious as the massive production of nitrate wastewater in chemical fertilizers, metallurgy and explosives industries [1,2]. The increased exposure of nitrate (NO_3^-) in aquatic ecosystems threat the human health and ecological balances [3–5]. Several technologies including ion exchange, biological denitrification, membrane filtration and electrodialysis have been developed to remove NO_3^- [6–9]. Electrocatalytic nitrate reduction (NO_3RR) to ammonia (NH_3) driven by renewable electricity resources represents a promising alternative, owing to green feature, mild reaction conditions and high reactivity [10–12]. More intriguingly, the produced NH_3-N could be recovered when coupled the electrochemical system with a membrane technology.

The catalyst is the core of the NO_3RR technology, which determines the kinetics, selectivity and energy consumption of the NO_3^- conversion to NH_3. TiO_2, as a typical transition metal oxide, is considered as a promising NO_3RR electrocatalyst owing to its abundance, high chemical stability and superior selectivity toward NH_3 in product [13–15]. Zhang *et al.* [16] and Niu *et al.* [17] reported the successful synthesis of TiO_2 applies to NO_3RR, and the NH_3 selectivity reaching to 87.1% and 81.9%, respectively. They further demonstrated that the O_V site on the TiO_2 surface was the reactive center for NO_3RR, and the exposed Ti^{3+} at the O_V site had a large affinity to both the NO_3^- and N-intermediates, which facilitated the proton-coupled electron transfer to reactants at electrode surface, and guaranteed the selective formation of NH_3-N [18]. Albeit the above advancements, there is still space for improvement in the NO_3RR performance of TiO_2 due to the following

* Corresponding authors.
E-mail addresses: junzhang@cqust.edu.cn (J. Zhang), jiangguangming@zju.edu.cn (G. Jiang).
[1] These authors contributed equally to this work.

https://doi.org/10.1016/j.cclet.2023.108410
1001-8417/

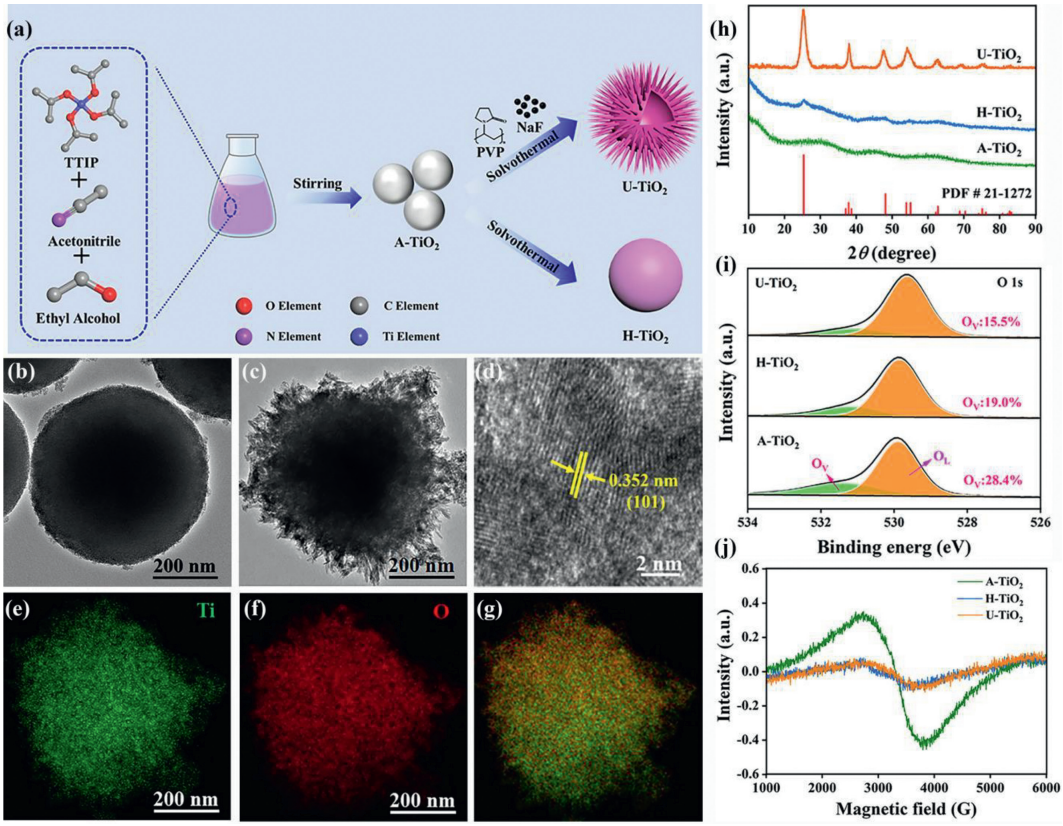

Fig. 1. (a) Schematic illustration for the synthesis of U-TiO_2, TEM images of (b) A-TiO_2 and (c) U-TiO_2, (d) HR-TEM image of U-TiO_2, (e-g) EDS elemental mapping images of U-TiO_2, (h) XRD patterns, (i) O 1s XPS spectra and (j) ESR spectra of as-synthesized A-TiO_2, H-TiO_2 and U-TiO_2.

two aspects. Firstly, the current NO_3RR kinetics suffers from an inferior mass transfer as the NO_3^- in the wastewater generally has a low concentration [19,20]. Furthermore, the NO_3^- with a negative charge bear a repulsive force from cathode owing to the electronic field, which makes it more difficult to approach the cathode [21–23]. On the other hand, the TiO_2, as a semiconductor, is poor in conductivity, which is actually unfavorable for the electrochemical system which urgently requires fast electron transfer [24–26,15].

Herein, we reported a facile approach to the surface O_V-enriched and urchin-like TiO_2 microparticles (U-TiO_2), which were used for NO_3RR. The NO_3RR performance, including NO_3^--N removal efficiency and kinetics, mass/specific activity, product distribution, durability, faradaic current efficiency and reaction pathway on U-TiO_2 were then evaluated under a combined electrochemical analyses and *in-situ* spectrometric study. To identify the reactive center and the contribution of NO_3^--N mass diffusion, O_V content, the NO_3RR performance of U-TiO_2 was also compared to a solid amorphous TiO_2 (A-TiO_2) that had close size but more surface O_V, and a solid sphere. Finally, the impacts of NO_3^- concentration, co-existing anions, and dissolved organic organisms in nitrate-laden water on the NO_3RR performance were also performed to assess its application in nitrogen remediation technique.

Fig. 1a illustrated the synthetic route to urchin-like TiO_2 catalyst (U-TiO_2). In this route, amorphous TiO_2 particles (A-TiO_2) were firstly prepared as precursors *via* the hydrolysis of TTIP in an NH_3 aqueous solution. They further evolved into U-TiO_2 when subjected to a hydrothermal treatment at 110 °C in the presence of F^- and PVP, which served as the etching and protecting agents, respectively [27]. In compared to the electrodeposition and electroshock methods, the developed method was more readily to succeed in controlling the morphology and structure of the TiO_2 particles [28,29]. The SEM images in Figs. S1 and S2 (Supporting information) and the TEM images in Figs. 1b and c revealed that the A-TiO_2 particle was a microsphere with smooth surfaces and a mean size of 600 nm, whereas the U-TiO_2 particles displayed unique urchin-like structures with particle size growing to approximately 630 nm. The HRTEM image in Fig. 1d revealed that the U-TiO_2 particle was composed of small crystalline domains with distinct lattice spacing of 0.352 nm, corresponding to the (101) planes of anatase phase [30,31]. The amorphous-anatase conversion during the hydrothermal process was also confirmed by the XRD patterns in Fig. 1h, where the characteristic diffraction peaks of anatase phase were discerned on U-TiO_2 (JCPDS No. 21–1272). Because the control test led to a relatively poor crystallinity in TiO_2 (denoted as H-TiO_2, TEM image shown in Fig. S3 in Supporting information), the substantial improvement in crystallinity from A-TiO_2 to U-TiO_2 would be also attributed to the presence of F^- and PVP [27]. The EDS elemental mapping results in Figs. 1e-g demonstrated the uniform distribution of Ti and O on U-TiO_2 and the absence of ionic impurities, such as F^-. The N_2 adsorption-desorption isotherm curves in Fig. S4 (Supporting information) revealed the mesoporous structures of the three TiO_2 samples. U-TiO_2 features a type-IV isotherm plot with a H3 hysteresis loop, while the A-TiO_2 and H-TiO_2 displayed type-I isotherm plots. On basis of the plot, the Brunauer–Emmett–Teller (BET) surface and pore size in these TiO_2 samples were estimated. Interestingly, the BET surface area of them followed a decreasing order of H-TiO_2 (586.3 m^2/g) ≈ A-TiO_2 (489.9 m^2/g) > U-TiO_2 (257.7 m^2/g), whereas their mean pore size exhibited a reverse order of U-TiO_2 (5.7 nm) > A-TiO_2 (2.2 nm) ≈ H-TiO_2 (2.5 nm). The much smaller BET surface area for urchin-like structure could be attributed to the enlarged pore size [31]. Albeit the decreased physical surface area, the large pore size, urchin-like structure would benefit for the exposure of active sites, the mass diffusion of dilute reactants and the electron transfer. Indeed, the

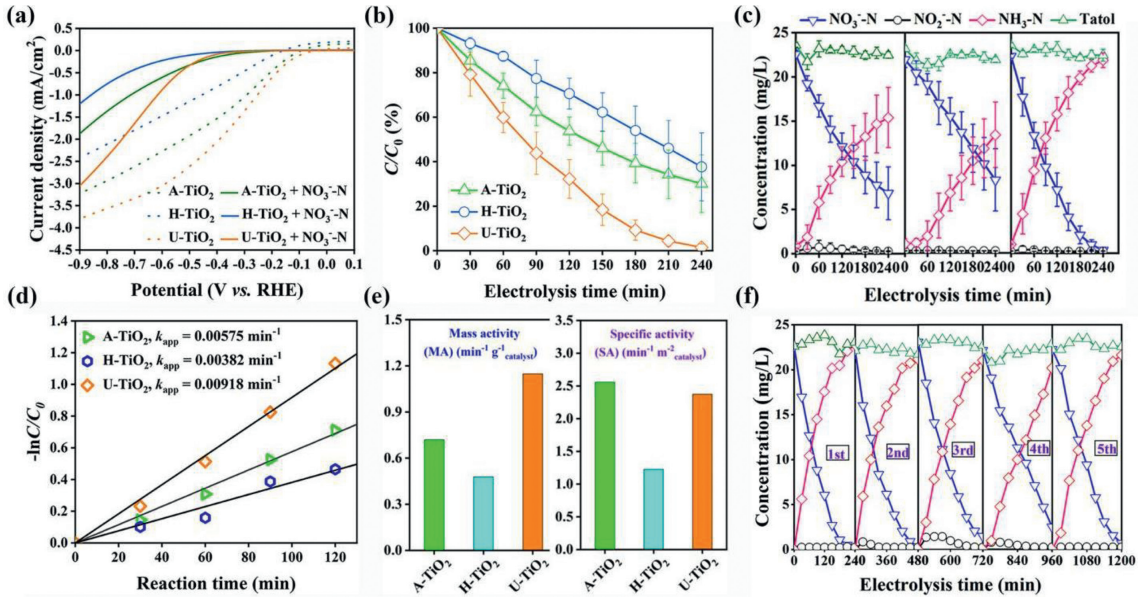

Fig. 2. Comparisons of (a) LSV in NO_3^--N-contained and NO_3^--N-free Na_2SO_4 electrolyte, (b) time-course C/C_0, (c) evolution in production distribution, (d) pseudo-first-order rate equation curves, (e) specific and mass activities between different cathodes in NO_3RR, (f) durability tests of U-TiO_2. Reaction conditions: [initial NO_3^--N] = 22.5 mg/L; cathodic potential = −0.60 V; electrolysis time = 240 min.

ECSA (Fig. S5 in Supporting information) of U-TiO_2 reached 92.1 m^2/g, much higher than that of H-TiO_2 (74.2 m^2/g) and A-TiO_2 (53.6 m^2/g). The presence of oxygen vacancy (O_V) in A-TiO_2, H-TiO_2 and U-TiO_2 was evidenced by the signal at $g = 2.004$ in ESR spectra and the O 1s XPS peak at 531.4 eV (Figs. 1i and j) [32–34]. A-TiO_2 should have a larger number of O_V due to the displayed stronger ESR signal and the stronger XPS peak for O_V. It was suggested that the hydrothermal process reduced the number of O_V, possibly due to the improved crystallinity.

To estimate the NO_3RR activity of catalysts, LSV tests in the electrolyte solution with and without NO_3^--N were conducted for A-TiO_2, H-TiO_2 and U-TiO_2, respectively. The dash LSV curves in Fig. 2a, obtained in the NO_3^--N-free solution, demonstrated a decreasing order of U-TiO_2 > A-TiO_2 > H-TiO_2 in the proton transfer kinetics at their surfaces according to the position of onset potential as well as the current density under the potential more negative than onset potential. After the addition of NO_3^--N, the onset potential for electrochemical reaction (the solid LSV curves) shifted negatively by around 0.30 V in compared to that in NO_3^--N-free solution for all the three catalysts. The abnormal phenomena could be ascribed to the fact of the hydrogen adsorption was hindered by the strong adsorption of NO_3^- on active sites, and the current response, assigned to NO_3^--N reduction, occurred under a more negative polarization potential. Furthermore, both the values of onset potential and current density for NO_3^--N reduction, as observed in the solid LSV curves, followed a decreasing order of U-TiO_2 > A-TiO_2 > H-TiO_2, suggesting the superior NO_3RR activity of U-TiO_2. To evaluate the performances of catalysts in removing NO_3^--N, potential-control batch NO_3RR tests were conducted in an Ar-saturated 50 mmol/L Na_2SO_4 solution with 22.5 mg/L NO_3^--N at −0.60 V *vs.* RHE (the same below). Fig. 2b displayed the reaction time-courses of C/C_0 (C denoted the NO_3^--N concentration) during NO_3RR on A-TiO_2, H-TiO_2 and U-TiO_2 respectively. As observed, all the three catalysts were active to remove the NO_3^--N, but obviously, the U-TiO_2 was the best with a NO_3^--N removal efficiency of 98.5% in 240 min of reaction, followed by the A-TiO_2 (62.3%) and H-TiO_2 (60.9%). Fig. 2c plotted the reaction time-dependent concentrations of NO_3^--N, NO_2^--N and NH_3-N as well as their total in the three reaction systems. As observed in the three reaction systems, the amount of NH_3-N kept continuous rising with the consumption of NO_3^--N. Intriguingly, the NO_2^--N, which was one common intermediate resolved during the conversion of NO_3^--N to NH_3-N, was evidenced in a very low yield (≤0.4 mg/L) during NO_3RR. As the NO_2^--N was one more toxic species than NO_3^--N, and its concentration was restricted under 1.0 mg/L by Standards for drinking water quality (GB5749–2022). The well control in NO_2^--N made the NO_3RR on our TiO_2-based catalysts a very safe process for practical environmental remediation of nitrate-contaminated water. On the other hand, the low NO_2^--N yield as well as the nearly constant total N content in solution indicated the high product selectivity towards NH_3-N. For example, the NH_3-N selectivity on U-TiO_2 reached 98.1%, which was the highest among the one reported in literatures (Table S1 in Supporting information).

The kinetics study revealed that the NO_3RR reaction on A-TiO_2, H-TiO_2 and U-TiO_2 all obeyed the pseudo-first-order mode ($\ln C/C_0 = -k_{app}\ t$) (Fig. 2d), suggesting that the NO_3RR was primarily limited by the mass diffusion of reactants. NO_3RR on U-TiO_2 was the fastest with a k_{app} = 9.18E-03 min^{-1}, followed by that on A-TiO_2 (5.75E-03 min^{-1}) and H-TiO_2 (3.82E-03 min^{-1}). On basis of the k_{app}, the mass (MA) and specific activities (SA) of the three catalysts were calculated. As observed in Fig. 2e, U-TiO_2 displayed the highest MA of 1.15 min^{-1} g_{cat}^{-1}, followed by A-TiO_2 (0.72 min^{-1} g_{cat}^{-1}) and H-TiO_2 (0.48 min^{-1} g_{cat}^{-1}). However, the SA of the catalysts followed a different order of A-TiO_2 (2.56 min^{-1} m_{cat}^{-2}) > U-TiO_2 (2.37 min^{-1} m_{cat}^{-2}) > H-TiO_2 (1.23 min^{-1} m_{cat}^{-2}). Given the lower ECSA of A-TiO_2, the higher SA but lower MA on A-TiO_2 suggested that the A-TiO_2 might have a higher density of active centers at surface than U-TiO_2. The underlying mechanism was discussed below. The faradaic current efficiency (F.E.%) of the three catalysts for NH_3-N production was also calculated. As shown in Fig. S6 (Supporting information), the U-TiO_2 delivered the largest one of 79.0%, followed by A-TiO_2 (59.7%) and H-TiO_2 (51.1%). The lower F.E.% than 100% in the three systems could be ascribed to the side hydrogen evolution reaction [35]. These results demonstrated that the NO_3RR on U-TiO_2 was more energy-efficient, and also safer due to the release of less explosive H_2. As a critical descriptor for efficient catalyst, the durability of U-TiO_2 for NO_3RR was also evaluated through repeated batch NO_3RR tests. The results in Fig. 2f revealed that U-TiO_2 could retain its high

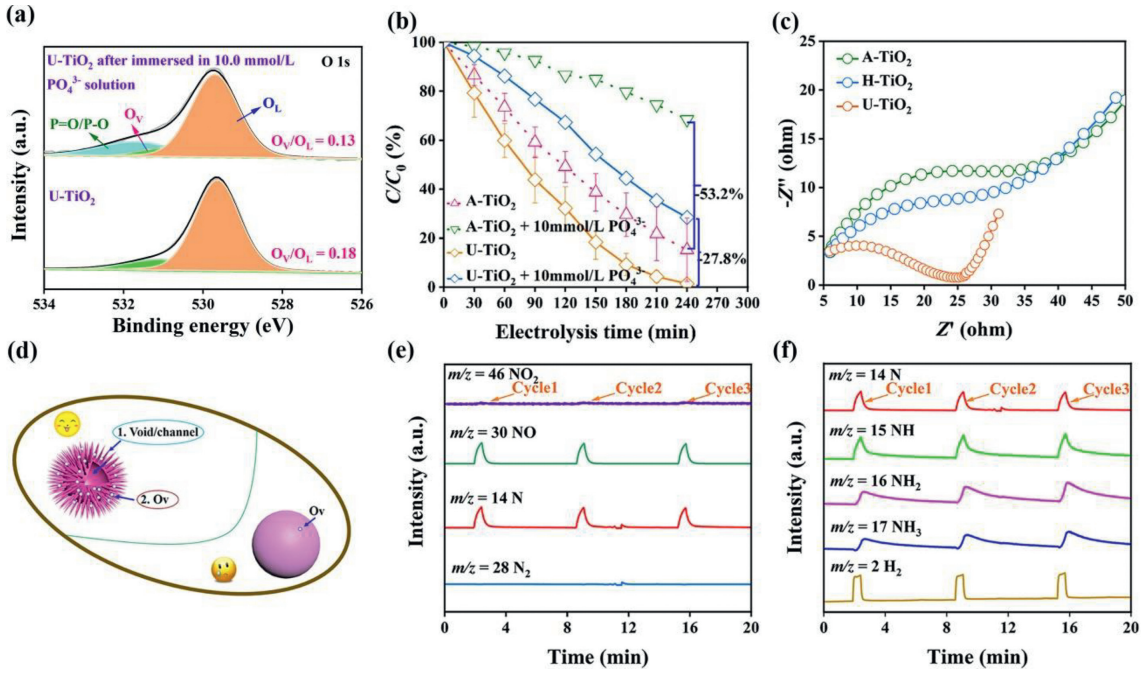

Fig. 3. (a) O 1s XPS spectra of U-TiO_2 after immersion in 10.0 mmol/L PO_4^{3-} solution. (b) NO_3RR performance of A-TiO_2 and U-TiO_2 before and after submerged in the PO_4^{3-} solution. (c) Nyquist plots of the samples. (d) Schematic illustration of the potential-dependent NO_3RR mechanism. (e, f) DEMS results of the NO_3RR on U-TiO_2.

performance after at least 5 consecutive cycles of reactions. The TEM image of the used U-TiO_2 in Fig. S7 (Supporting information) showed that the catalyst kept its urchin-like structure as well as the exposure of the (101) facet of anatase. Furthermore, the O 1s XPS spectra in Fig. S8 (Supporting information) evidenced the preservation of O_V on the used U-TiO_2, suggesting that the O_V could be *in-situ* regenerated under the reductive potential of NO_3RR.

Previous researches had verified that the O_V sites with exposed Ti^{3+} species were the primary reactive centers of TiO_2-based catalysts for NO_3RR [16]. To probe into the role of O_V in our system, the NO_3RR performances of U-TiO_2 and A-TiO_2 before and after the quench of their surface O_V through immersing the cathodes in 10.0 mmol/L PO_4^{3-} solution prior to reaction were all examined [36]. As presented in Fig. 3a, after being treated in 10.0 mmol/L PO_4^{3-}, the O_V/O_L ratio on U-TiO_2 was indeed reduced from initial 0.18 to 0.13, owing to the occupation of O_V by PO_4^{3-} *via* Ti^{3+}-PO_4^{3-} complexation [37]. Correspondingly, the NO_3^--N removal efficiency for the O_V-quenched U-TiO_2 dropped by 27.8%, in compared to that of the fresh U-TiO_2 (Fig. 3b). All these clearly verified the critical role of O_V as reactive centers on our TiO_2 catalyst. Fig. 3b also showed that the NO_3^--N removal efficiency on the O_V-quenched A-TiO_2 was reduced by a larger extent of 53.2% in compared to that on fresh A-TiO_2. The displayed more significant efficacy of O_V on A-TiO_2 indicated a larger density of O_V at its surface, which was consistent with the XPS results in Fig. 1i. Given the critical role of O_V in NO_3RR, the large density of surface O_V on A-TiO_2 would rationalize why A-TiO_2 had a larger SA than U-TiO_2 (Fig. 2e).

Though A-TiO_2 had a larger number of O_V on surface, its MA was still lower than that of U-TiO_2. This suggested that besides the number of active sites (*i.e.*, O_V), the NO_3RR performance on U-TiO_2 depended on other factors, such as the charge transfer at catalyst/water interfaces. The Nyquist plots in Fig. 3c revealed an increasing order of U-TiO_2 < H-TiO_2 < A-TiO_2 in charge transfer resistance at catalyst/water interfaces [38]. Intriguingly, this order was exactly opposite to that of their MA, indicating that the NO_3RR performance was primarily associated with the charge transfer rate at catalyst surface. Generally, the semiconductor with more defects or in amorphous structure usually displayed higher electronic conductivity. The U-TiO_2, with high crystallinity and less defects, would have inferior electronic conductivity to A-TiO_2. Accordingly, the low charge resistance at U-TiO_2/water interfaces should benefit from the urchin-like hierarchical structure, which provided abundant channels/voids for mass diffusion and also exposed more reactive centers for charge transfer [27,39,40]. All these demonstrated that the superior NO_3RR performance on U-TiO_2 originated from the reproducible O_V site (reactive center) as well as the urchin-like structure (Fig. 3d). Notably, the urchin-like structure took the leading contribution in our system.

To get more knowledge about the NO_3RR on U-TiO_2, the NO_3RR pathway was explored with *in-situ* DEMS test, which could resolve the reaction intermediates during the conversion of NO_3^--N to NH_3-N, even when the intermediates were of a short lifetime. As demonstrated in Figs. 3e and f, the *m/z* signals for 2, 14, 15, 16, 17, and 30 were discerned under a working potential of −0.60 V, which could be assigned to H_2, N, NH, NH_2, NH_3, and NO species, respectively. No *m/z* signals for N_2 and NO_2 were captured, indicating the inferior selectivity of NO_3^- conversion to N_2 on U-TiO_2. This was consistent with our experimental results that little N_2 was produced. On basis of the resolved species and the detected product in aqueous solution, we could propose a NO_3RR pathway of $^*NO_3^- \rightarrow {}^*NO_2^- \rightarrow {}^*NO \rightarrow {}^*N \rightarrow {}^*NH \rightarrow {}^*NH_2 \rightarrow {}^*NH_3$ on U-TiO_2 surface (* denotes the reactive sites on catalyst). Such a pathway of NO_3^--NH_3 conversion was also reported on many O_V-triggered NO_3RR systems, which, therefore, solidified that the O_V on TiO_2 was the primary reaction centers.

To assess the application of U-TiO_2-driven NO_3RR on different scenarios, the NO_3RR performances of U-TiO_2 were investigated under different NO_3^--N feeding concentrations. The results in Fig. 4a showed that with the feeding concentrations increasing from 22.5 mg/L to 90.0 mg/L, more NO_3^--N are remained after a reaction of 240 min. Corresponding NO_3^--N removal efficiency ($(1\text{-}C/C_0) \times 100\%$) was found to decrease from initial 98.5% to 46.1%. However, as observed in Fig. 4b, the NH_3 yield at the end of reaction increased with the feeding NO_3^--N concentra-

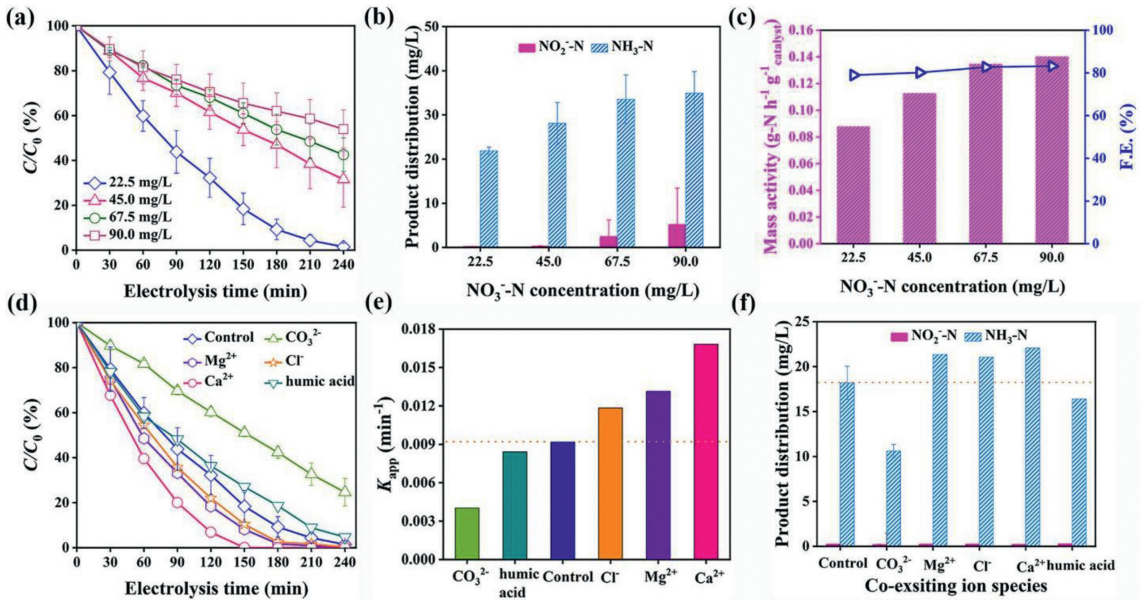

Fig. 4. Effects of (a-c) initial NO_3^--N concentration on NO_3^--N removal, evolution in production distribution, MA and F.E.%. (d-f) The presence of coexisting ions on NO_3^--N removal, *pseudo*-first-order rate equation curves for NO_3RR, and evolution in production distribution over U-TiO_2. Reaction conditions: [initial NO_3^--N] = 22.5 mg/L for (d-f); cathodic potentiall = −0.60 V; electrolysis time = 240 min for all the tests.

tion, indicating that more NO_3^--N was converted to NH_3-N when fed a higher concentration. These results supported the conclusion that the NO_3RR kinetics on U-TiO_2 under a NO_3^--N concentration range of 22.5∼90.0 mg/L was limited by the mass diffusion of NO_3^-. Generally, a higher NO_3^--N concentration would promote the collision frequency between NO_3^--N and catalyst, contributing to an accelerated NO_3RR [6]. Additionally, Fig. 4b also revealed that more NO_2^--N was produced with the increase in feeding NO_3^--N concentration. This might be ascribed to the fact that the NO_3^- would compete the reactive centers with NO_2^-, some of which was squeezed off the reactive centers before being hydrogenated to NH_3. Given the large toxicity of NO_2^-, this result reminded us to carefully optimize the reaction conditions when dealing with the wastewater with concentrated NO_3^--N. Fortunately according to our previous work, prolonging the reaction time could be an efficient way to control the residue of NO_2^- in solution [41]. Fig. 4c also compared the F.E.% for NH_3-N production on U-TiO_2 under different NO_3^--N concentrations. It was revealed that the F.E.% depended less on the feeding NO_3^--N concentration. This was unexpected as an enhanced NO_3^--NH_3 conversion was usually accompanied with a larger F.E.% [42]. The underlying mechanism will be explored in the future work.

As most of the industrial processes employed natural water as water resources, the resultant wastewater usually contained some impurity ions (*e.g.*, Cl^-, CO_3^{2-}, Mg^{2+} and Ca^{2+}) and natural organic materials (NOM), which might pose some effects on the electrochemical process. Herein their effects on the NO_3RR performance of U-TiO_2 were investigated under a potential of −0.60 V. Humic acid was introduced as the representative of NOM. The concentrations of the impurities were set according to the values of them in natural water, such as Cl^- (5.0 mmol/L), CO_3^{2-} (1.0 mmol/L), Mg^{2+} (1.0 mmol/L) and Ca^{2+} (2.0 mmol/L), and humic acid (3.3 mg/L) [43]. Fig. 4d revealed that the presence of Ca^{2+}, Mg^{2+} and Cl^- promoted NO_3RR, due to the faster drop in C/C_0 in compared to that in the control experiment. On basis of the C/C_0 value at 150 min, we could tell that the Ca^{2+} was the most efficient species in promoting NO_3RR, followed by Mg^{2+} and Cl^-. In contrast, the inclusion of CO_3^{2-} and humic acid slowed down the NO_3RR. The detrimental effects of CO_3^{2-} was more significantly as the C/C_0 at the end of reaction remained 75.4%. Fig. S9 (Supporting information) showed that the NO_3RR on U-TiO_2 still obeyed the *pseudo*-first-order reaction mode, indicating that the mass diffusion of NO_3^- continued to be the rate-determined step for NO_3RR even when the NO_3RR was boosted in a significant extent in the presence of Ca^{2+}. Fig. 4e summarized the k_{app}, which followed a decreasing order of Ca^{2+} > Mg^{2+} > Cl^- > Control > humic acid > CO_3^{2-}. Fig. 4f compared the products of NO_3RR at 150 min in the presence of impurity ions and humic acid. As observed, the inclusion of Ca^{2+}, Mg^{2+} and Cl^- produced more NH_3-N, while the presence of humic acid and CO_3^{2-} reduced yield of NH_3-N, both of which was consistent with the displayed efficacy of them on NO_3RR kinetics. All these suggested that the impurity species affects primarily on the kinetics of NO_3^--N conversion to NH_3-N rather than the reaction pathway. Fig. 4f also showed that the NO_2^--N yields in all the investigated systems were kept under a low level, even when the NO_3RR was hindered under a large extent in the presence of CO_3^{2-}. The underlying mechanism was unclear, but this unique feature was appealing as our U-TiO_2 had a strong resistant to water quality in the aspect of the well control in NO_2^--N yield.

The detrimental effects of humic acid and CO_3^{2-} on O_V-driven catalysis had been documented in literature, which could attributed to the strong complexation effect between the carboxyl group and the exposed cation at the O_V site (*i.e.*, the Ti^{3+}), leading to the poisoning of the reactive centers [44,41]. The promoting effects of Ca^{2+} and Mg^{2+} and Cl^- were unexpected. In general, the NO_3^- with a negative charge suffered a repulsive force from cathode owing to the electronic field, which raised extra energy for them to approach electrode for NO_3RR. We speculated that the presence of Ca^{2+} and Mg^{2+} might alter the structure of double electric layer at electrode/solution interface by forming an instantaneous neutral ion pair, which, as a result, weakened the repulsive force between NO_3^- and the cathode [45]. In the future, more efforts will be devoted to unraveling the interactions between the impurity ions and the performance of the catalyst.

Herein, we developed a defective urchin-like TiO_2 microparticles catalyst for NO_3RR. When subjected to 22.5 mg/L of NO_3^--N, it could afford a mass activity of 1.15 min^{-1} $mg^{-1}_{catalyst}$, a low yield of toxic NO_2^--N intermediate (≤0.4 mg/L) and an exceptional high NH_3-N selectivity of 98.1% under the working potential of −0.60 V, outperforming most of the reported catalysts. We also

demonstrated that the O_V was the real reactive sites for NO_3RR, but rather than its content, the NO_3RR kinetics were more dependent on the urchin-like structure, which was beneficial for the interfacial electron transfer of TiO_2 and the mass diffusion of NO_3^--N around TiO_2. The *in-situ* DEMS test revealed that the NO_3RR on U-TiO_2 followed a pathway of $^*NO_3^- \rightarrow {}^*NO_2^- \rightarrow {}^*NO \rightarrow {}^*N \rightarrow {}^*NH \rightarrow {}^*NH_2 \rightarrow {}^*NH_3$. The U-$TiO_2$ could keep its robust performance under a wide NO_3^--N concentration range and in the presence of Ca^{2+}, Cl^- and Mg^{2+}. However, the humic acid and CO_3^{2-} in wastewater posed detrimental effects on NO_3RR.

Declaration of competing interest

The authors declare that they have no known competing financial interests or personal relationships that could have appeared to influence the work reported in this paper.

Acknowledgments

The authors acknowledge the financial support by National Natural Science Foundation of China (Nos. 22176019, 51978110), the Science and Technology Research Program of Chongqing Municipal Education Commission (Nos. KJQN201800829, KJQN201900837, KJZD-K202000802, KJQN201901527), Chongqing Research Student Science and Technology Innovation Project (No. CYS22724), Innovation and Entrepreneurship Training Plan for College Students (No. 202111799007).

Supplementary materials

Supplementary material associated with this article can be found, in the online version, at doi:10.1016/j.cclet.2023.108410.

References

[1] X. Zou, J. Xie, C. Wang, et al., Chin. Chem. Lett. 34 (2023) 107908.
[2] Z.Y. Wu, M. Karamad, X. Yong, et al., Nat. Commun. 12 (2021) 2870.
[3] T. Feng, F. Li, X. Hu, et al., Chin. Chem. Lett. 34 (2023) 107862.
[4] J. Lim, C.Y. Liu, J. Park, et al., ACS Catal. 11 (2021) 7568–7577.
[5] F. Ni, Y. Ma, J. Chen, et al., Chin. Chem. Lett. 32 (2021) 2073–2078.
[6] T. Zhu, Q. Chen, P. Liao, et al., Small 16 (2020) 2004526.
[7] Y. Wang, W. Zhou, R. Jia, et al., Angew. Chem. Int. Ed. 59 (2020) 5350–5354.
[8] C.A. Clark, C.P. Reddy, H. Xu, et al., ACS Catal. 10 (2020) 494–509.
[9] S. Xu, Y. Shi, Z. Wen, et al., Appl. Catal. B: Environ. 323 (2023) 122192.
[10] D. Chen, S. Zhang, X. Bu, et al., Nano Energy 98 (2022) 107338.
[11] J.N. Gao, N. Shi, Y.F. Li, et al., Environ. Sci. Technol. 56 (2022) 11602–11613.
[12] J.N. Gao, N. Shi, X.B. Guo, et al., Environ. Sci. Technol. 55 (2021) 10684–10694.
[13] X. Zhang, C. Wang, Y. Guo, et al., J. Mater. Chem. A 10 (2022) 6448–6453.
[14] D.E. Kim, D. Pak, Chemosphere 228 (2019) 611–618.
[15] J. Chen, X. He, D. Zhao, et al., Green Chem. 24 (2022) 7913–7917.
[16] R. Jia, Y. Wang, C. Wang, et al., ACS Catal. 10 (2020) 3533–3540.
[17] Z. Wei, X. Niu, H. Yin, et al., Appl. Catal. A: Gen. 636 (2022) 118596.
[18] H. Hirakawa, M. Hashimoto, Y. Shiraishi, et al., J. Am. Chem. Soc. 139 (2017) 10929–10936.
[19] W.J. Sun, H.Q. Ji, L.X. Li, et al., Angew. Chem. Int. Ed. 60 (2021) 22933–22939.
[20] Z. Song, Y. Liu, Y. Zhong, et al., Adv. Mater. 34 (2022) 2204306.
[21] X. Fu, J. Zhang, Y. Kang, Chem. Catal. 2 (2022) 2590–2613.
[22] T.H. Jeon, Z.Y. Wu, F.Y. Chen, et al., J. Phys. Chem. C 126 (2022) 6982–6989.
[23] L. Li, C. Tang, X. Cui, et al., Angew. Chem. Int. Ed. 60 (2021) 14131–14137.
[24] C. Liang, P. Li, Y. Zhang, et al., J. Power Sources 372 (2017) 235–244.
[25] S. Gu, A.N. Marianov, H. Xu, et al., J. Mater. Sci. Technol. 80 (2021) 20–27.
[26] X. Lu, Y. Wang, J. Huang, et al., Chem. Eng. J. 434 (2022) 134648.
[27] J.H. Pan, X.Z. Wang, Q. Huang, et al., Adv. Funct. Mater. 24 (2014) 95–104.
[28] J. Kim, H. Kim, G.H. Han, et al., Exploration 2 (2022) 20210077.
[29] L. Du, H. Xiong, H. Lu, et al., Exploration 2 (2022) 20210363.
[30] T. Wu, H. Zhao, X. Zhu, et al., Adv. Mater. 32 (2020) 2000299.
[31] L. Deng, B. Chang, D. Shi, et al., Renew. Energ. 170 (2021) 858–865.
[32] P.S. Murphin Kumar, V.K. Ponnusamy, K.R. Deepthi, et al., J. Mater. Chem. A 6 (2018) 23435–23444.
[33] J. Wang, M. Xu, J. Zhao, et al., Appl. Catal. B: Environ. 237 (2018) 228–236.
[34] L. Huang, D. Li, J. Liu, et al., Y. Feng, J. Hazard. Mater. 393 (2020) 122329.
[35] J. Sun, W. Gao, H. Fei, et al., Appl. Catal. B: Environ. 301 (2022) 120829.
[36] X. Lv, K. Jiang, H. Wu, et al., ACS EST Water 2 (2022) 1451–1460.
[37] F.o. Ahimou, C.J.P. Boonaert, Y. Adriaensen, et al., J. Colloid Interf. Sci. 309 (2007) 49–55.
[38] P. Kuang, Y. Wang, B. Zhu, et al., Adv. Mater. 33 (2021) 2008599.
[39] H. Shin, H.-i. Kim, D.Y. Chung, et al., ACS Catal. 6 (2016) 3914–3920.
[40] D.C. Nguyen, T.L. Luyen Doan, S. Prabhakaran, et al., Nano Energy 82 (2021) 105750.
[41] G. Jiang, M. Peng, L. Hu, et al., Chem. Eng. J. 435 (2022) 134853.
[42] X. Zhang, Y. Wang, C. Liu, et al., Chem. Eng. J. 403 (2021) 126269.
[43] B.P. Chaplin, E. Roundy, K.A. Guy, et al., Environ. Sci. Technol. 40 (2006) 3075–3081.
[44] Z. Mao, L. Liu, H.B. Yang, et al., Electrochim. Acta 391 (2021) 138886.
[45] R.R. Nazmutdinov, D.V. Glukhov, G.A. Tsirlina, et al., J. Electroanal. Chem. 582 (2005) 118–129.